A spin qubit in a fin field-effect transistor

Leon C. Camenzind,[1,*] Simon Geyer,[1,*] Andreas Fuhrer,[2] Richard J. Warburton,[1] Dominik M. Zumbühl,[1,†] and Andreas V. Kuhlmann[1,2,†]

[1] *Department of Physics, University of Basel, Klingelbergstrasse 82, CH-4056 Basel, Switzerland*

[2] *IBM Research-Zürich, Säumerstrasse 4, CH-8803 Rüschlikon, Switzerland*

(Dated: March 15, 2021)

Quantum computing's greatest challenge is scaling up. Several decades ago, classical computers faced the same problem and a single solution emerged: very-large-scale integration using silicon. Today's silicon chips consist of billions of field-effect transistors (FinFETs) in which current flow along the fin-shaped channel is controlled by wrap-around gates. The semiconductor industry currently employs fins of sub-10 nm width, small enough for quantum applications: at low temperature, an electron or hole can be trapped under the gate and serve as a spin qubit. An attractive benefit of silicon's advantageous scaling properties is that quantum hardware and its classical control circuitry can be integrated in the same package. This, however, requires qubit operation at temperatures greater than 1 K where the cooling is sufficient to overcome the heat dissipation. Here, we demonstrate that a silicon FinFET is an excellent host for spin qubits that operate even above 4 K. We achieve fast electrical control of hole spins with driving frequencies up to 150 MHz and single-qubit gate fidelities at the fault-tolerance threshold. The number of spin rotations before coherence is lost at these "hot" temperatures already matches or exceeds values on hole spin qubits at mK temperatures. While our devices feature both industry compatibility and quality, they are fabricated in a flexible and agile way to accelerate their development. This work paves the way towards large-scale integration of all-electrical and ultrafast spin qubits.

Quantum dot (QD) spin qubits [1, 2] in silicon (Si) have great potential for application in large-scale quantum computation [3], owing to their long coherence times [4] and high quality factors [5–7]. Moreover, state-of-the-art complementary metal-oxide-semiconductor (CMOS) manufacturing processes [8–10] can be employed to engineer a dense array of interconnected spin qubits [11, 12]. Inspired by the great success of conventional integrated circuits, on-chip integration of the classical control electronics with the qubit array has been proposed to overcome the challenge in wiring up large numbers of multi-terminal QD devices [13]. Since the electronics produce heat, the amount of control functionality that can be implemented strongly depends on the available cooling power.

* These authors contributed equally to this work;

† e-mail: dominik.zumbuhl@unibas.ch, andreas.kuhlmann@unibas.ch

Therefore, it is highly beneficial to operate qubits at temperatures greater than 1 K, where cooling power is orders of magnitude higher than at mK temperatures [14, 15]. For instance, Intel's cryogenic control chip named Horse Ridge works at 3 K [16].

Spin qubits come in two distinct flavours: electron [4–6, 14, 15, 17] and hole [8, 18–22]. While for electrons an artificial spin-orbit interaction (SOI) can be engineered by equipping the qubit with a micromagnet [5, 6, 17], hole spins experience a strong intrinsic SOI [23]. All-electrical spin control is achieved via electric-dipole spin resonance (EDSR) [24–31], where an applied oscillating electric field induces spin rotations. For holes, in comparison to electrons, no additional device components are required, which reduces device complexity for the benefit of scalability. Furthermore, for holes in Si nanowires or fin field-effect transistors (FinFETs) the SOI can be exceptionally strong and fully tunable, allowing for a switchable coupling strength and a way to mitigate the effects of charge noise [22, 23, 32]. Moreover, hole spins are better protected against nuclear spin noise due to their weak hyperfine interaction [33, 34].

Recently, electron spin qubits operating up to 1.5 K have been demonstrated [14, 15]. Here we show hole spin qubits working at 1.5 to 5 K, that is, in a temperature range where the thermal energy is much larger than the qubit level splitting and cryogenic control electronics can be operated [16]. The hole spin qubits are integrated in Si FinFET devices that are realised utilising standard CMOS fabrication techniques, such as self-aligned gates and chemically-selective plasma etches instead of lift-off processes [9, 10]. In addition, a high degree of process flexibility and a short turnaround are achieved by using electron-beam instead of advanced optical lithography [35]. The fin provides a one-dimensional confinement for the holes, enabling fast and electrically tunable effective spin-1/2 qubits [22, 23, 32]. We demonstrate EDSR-based spin control with Rabi frequencies up to 150 MHz and voltage-tunable qubit frequencies, a feature employed to implement z-rotations as fast as 45 MHz. Moreover, we show spin rotations around the x- and y-axis of the Bloch sphere with a single-qubit gate fidelity of 98.9 % at 1.5 K. A high robustness against temperature allows for qubit operation above the boiling point of liquid ^{4}He, albeit with a slightly reduced dephasing time T_2^* compared to 1.5 K, which is consistent with an observed whitening of the spectral noise density on increasing temperature.

A scanning electron microscope (SEM) tilted side-view and a transmission electron microscope (TEM) cross-sectional view of a co-fabricated device are shown in Figs. 1a,b. Since these FinFETs are fabricated using CMOS processes, they feature a highly uniform gate profile [35] and an ultra-small gate pitch [10]. By negatively biasing the gate electrodes, an accumulation-mode hole double quantum dot (DQD), hosting two individual spin-1/2 qubits, is formed [10]. We measure the

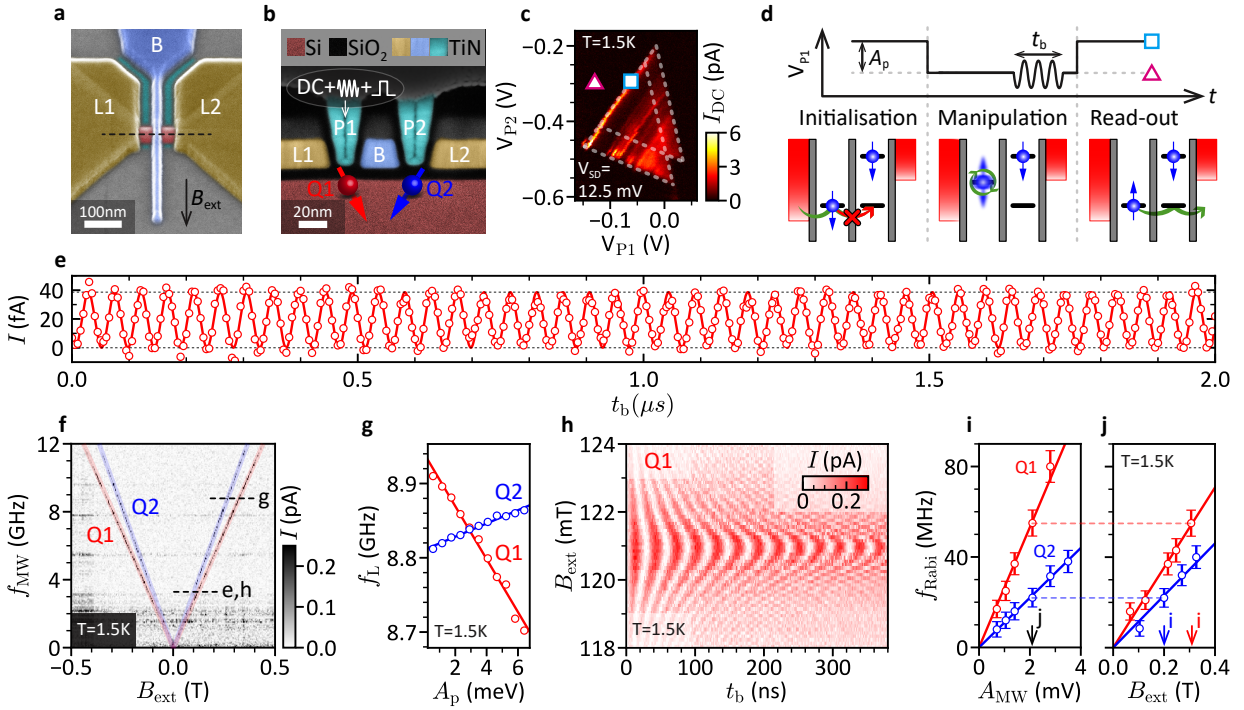

FIG. 1. **Spin-orbit qubits in a FinFET. a**, False-colour SEM image of an unfinished device showing the two lead gates L1, L2 (yellow) as well as the inter-dot barrier gate B (blue, $\simeq 35\,\mathrm{nm}$). An in-plane external magnetic field B_{ext} is applied perpendicular to the fin (red). **b**, Cross-sectional TEM image along the black dashed line shown in **a** after integration of the QDs' plunger gates P1, P2 (turquoise, $\simeq 15\,\mathrm{nm}$). In addition to a DC voltage, fast pulses and microwaves can be applied to P1. **c**, Measurement of a spin-blocked pair of bias triangles. The blue square and pink triangle mark the qubit initialisation/readout and manipulation point, respectively. **d**, Schematic illustration of the spin manipulation cycle with corresponding pulse scheme. **e**, Rabi oscillation with $f_{\mathrm{Rabi}} = 22\,\mathrm{MHz}$ measured on Q1 at $B_{\mathrm{ext}} = 123\,\mathrm{mT}$, $f_{\mathrm{MW}} = 3.311\,\mathrm{GHz}$, $A_{\mathrm{MW}} = 1.1\,\mathrm{mV}$ and $\mathrm{T} = 1.5\,\mathrm{K}$. The data has been corrected by removing a small constant offset, and is fitted (solid curve) to $I(t_{\mathrm{b}}) = A\sin(2\pi f_{\mathrm{Rabi}} t_{\mathrm{b}} + \theta) + B$ with A, B, f_{Rabi} and θ as fit parameters. **f**, Measurement of the current as a function of f_{MW} and B_{ext}. Along the red (blue) line the spin resonance condition is met for Q1 (Q2). For each frequency the average current has been subtracted. **g**, Electrical tunability of the qubit frequency with the depth of the Coulomb pulse. Solid lines represent linear fits to the data. **h**, Detuned Rabi oscillations showing a typical chevron pattern, measured at $f_{\mathrm{MW}} = 3.311\,\mathrm{GHz}$ and $A_{\mathrm{MW}} = 1.4\,\mathrm{mV}$. Dependence of f_{Rabi} on A_{MW} **j** and B_{ext} **i**. Solid lines are linear fits to the data with zero offset.

direct current I_{DC} through the DQD, which when combined with spin-to-charge conversion through Pauli spin blockade (PSB) [36, 37] provides qubit readout functionality (for further details on the device and measurement setup see Methods). For the device investigated, PSB is observed for the $(1,1) \rightarrow (0,2)/(2,0)$ charge state transitions and no additional transitions are observed when further depleting the quantum dots (QDs). Here (n_1, n_2) denotes the charge state with n_1/n_2 holes

in the left/right QD. This observation strongly suggests that the DQD operates in the two-hole regime (Supplementary Section 2); an on-chip charge sensor would prove this [38, 39].

In the PSB regime hole tunnelling is forbidden by spin conservation if the two spins, occupying a $(1,1)$ charge state, are aligned parallel ($|\uparrow\uparrow\rangle$ or $|\downarrow\downarrow\rangle$). This blockade, however, can be lifted by flipping the direction of one hole spin using EDSR [8, 19, 22, 25, 27], which is performed by applying square voltage pulses and microwave (MW) bursts to gate P1 (Fig. 1b). The measurements consist of three stages (Figs. 1c,d): first, the two holes spins are initialised in a polarised spin state through PSB. Then, the system is pulsed into Coulomb blockade, where the MW signal is applied. Finally, in the readout stage a current is detected if the spins are antiparallel, such that one hole can tunnel to the neighbouring QD and exit to the nearby reservoir (Supplementary Section 1).

For high-temperature operation of spin qubits [14, 15], spin-to-charge conversion via PSB rather than energy-selective tunnelling [40] is favourable, since the single-dot singlet-triplet splitting [10] is typically much larger than the Zeeman energy. Thus, the measurements can be performed at higher temperature and smaller external magnetic field, resulting in lower and technically less demanding qubit frequencies.

EDSR takes place under the condition that the MW frequency f_{MW} equals the Larmor frequency $f_L = |g^*|\,\mu_B\,|B_{\mathrm{ext}}|/h$, where g^* denotes the effective hole Landé g^*-factor along the magnetic field B_{ext} direction, μ_B Bohr's magneton and h Planck's constant. In Fig. 1f the resonance appears as a V-shape that maps out f_L in the f_{MW}-B_{ext} plane. The single-hole spin resonance conditions differ slightly for the two qubits (Q1, Q2), making them individually addressable. From the slope of the current lines, we extract absolute values for the g^*-factor of 1.94 ± 0.05 and 2.35 ± 0.05, respectively. These two different values indicate a sensitivity to the local electric fields, which also provides an additional control knob for the g^*-factor, and thus the qubit frequency [4, 6, 20, 22, 31]. This is confirmed by Fig. 1g, where the f_L-dependence on the square pulse amplitude A_{p} is shown.

When the MW drive is on resonance, the DQD current reveals Rabi oscillations as a function of the burst duration t_{b}. An example of a 22 MHz Rabi oscillation, whose decay time is too long to be observed within $87\,\pi$ rotations, is given in Fig. 1d. For a detuned f_{MW} the qubit rotates around a tilted axis on the Bloch sphere, resulting in faster rotations of reduced contrast as demonstrated by the chevron pattern seen in Fig. 1h. The Rabi frequency f_{Rabi} increases linearly not only with the MW amplitude A_{MW} (Fig. 1i), but also B_{ext} (Fig. 1j) as expected for SOI-mediated spin rotations [22, 24, 25, 29–31]. For these measurements, A_{MW} is calibrated using the photon-assisted-tunnelling response (Supplementary Section 3) [25]. The maximum f_{Rabi} observed is 147 MHz (Supplementary Section 5), which corresponds to a spin-flip time of just ~ 3.4 ns. While the faster Rabi oscillations

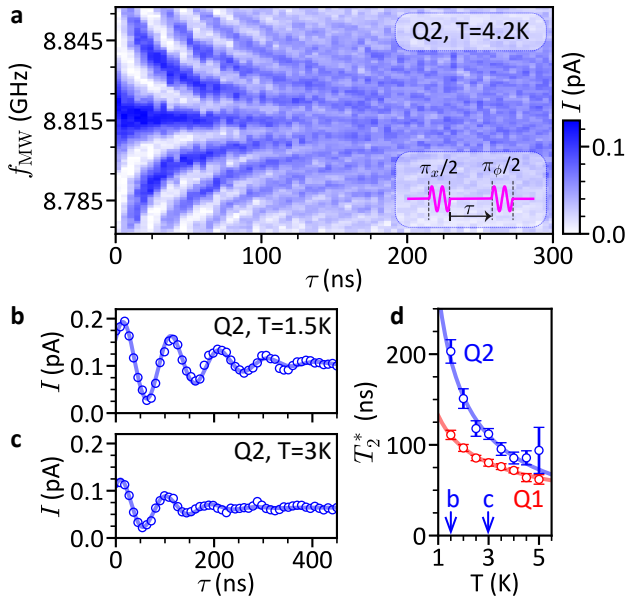

FIG. 2. **Hot qubit coherence. a,** Ramsey-fringe experiment performed at 4.2 K. $B_{\rm ext}$ is fixed at 267 mT. The pulse sequence, which consists of two 15 ns-long $\frac{\pi}{2}$-bursts separated by the waiting time τ, is illustrated in the bottom right inset. ϕ denotes the phase of the second pulse with respect to the first one, here $\phi = 0$. Decay of Ramsey fringes at 1.5 K **b** and 3 K **c**. The data were taken on resonance with a τ-dependent phase $\phi(\tau)$, which adds an artificial oscillation [41]. Solid curves show fits to $A+B\sin(\omega\tau+\theta)\exp[-(\tau/T_2^*)^{\beta+1}]$ with temperature dependent β. **d**, Temperature dependence of the spin dephasing time revealing a power-law decay $T_2^* \propto \mathrm{T}^{-\eta}$, where $\eta = 0.46 \pm 0.02$ for Q1 and $\eta = 0.81 \pm 0.06$ for Q2, respectively.

suggest that Q1 is hosted by the left QD, which is closer to the MW drive, this assignment has to be taken with a grain of salt. Under the assumption that EDSR occurs due to a periodic displacement of the wave function as a whole, the g^*-factor is not modulated [31] and $f_{\rm Rabi}$ also depends on the respective QD size and spin-orbit length $l_{\rm SO}$ [25]. We can therefore state an estimate for $l_{\rm SO}$ in the range of 20 to 60 nm (Supplementary Section 6), that is, similar values to the one reported before [10] and in very good agreement with theory predictions [23]. An effective dot size of $\sim$5.7 (7.1) nm is extracted from the single-dot singlet-triplet splitting for the left (right) QD [10].

A key parameter for the qubit controllability is the quality factor defined as $\mathrm{Q} = 2 f_{\rm Rabi} T_2^{\rm Rabi}$, where $T_2^{\rm Rabi}$ is the decay time of the Rabi oscillations. For the data presented in Fig. 1e no decay is observed within $\sim 2\,\mu$s, that is, $\mathrm{Q} \gg 87$. In terms of quality factors, our hole spin qubits therefore outperform their hot electron counterparts [14, 15] and even state-of-the-art planar Si-MOS QD qubits at mK temperatures [4].

Next, we evaluate the spin coherence by performing a Ramsey experiment. Here, two $\frac{\pi}{2}$-pulses separated by a delay time τ during which the qubit can freely evolve and dephase are applied. When

f_{MW} is detuned from the qubit resonance, the current through the device shows coherent oscillations known as Ramsey fringes. The data of Fig. 2a is measured at a temperature of T = 4.2 K, which corresponds to the boiling point of liquid ^{4}He, and which can be achieved by immersing the sample in a liquid ^{4}He bath or at the second stage of a dry pulse-tube refrigerator. Both options provide an immense resource for cooling in a technically non-demanding way. The dephasing time T_2^* is determined by fitting the envelope of the fringe decay to $\exp(-(\tau/T_2^*)^{\beta(\mathrm{T})+1})$, where β depends on temperature as discussed later. Despite the fact that our qubit readout is protected against temperature by the large orbital energies, which exceed the thermal energy available at 4.2 K by an order of magnitude, a degradation of the signal contrast on increasing temperature is observed (Fig. 2b,c). The reasons for this are not yet fully understood (Supplementary Section 7). The T-dependence of T_2^* in the range of 1.5 to 5 K is presented for both qubits in Fig. 2d. While Q1 can be manipulated faster than Q2, it lags behind in coherence. The spin dephasing time drops with increasing temperature, described by a power-law decay $\propto \mathrm{T}^{-\eta}$ with $\eta = 0.5$ (0.8) for Q1 (Q2), a rather weak temperature dependence similar to previous reports [14, 15]. The obtained values for T_2^* are consistent with the EDSR spectral width (Supplementary Section 8). In the following the focus is on the more coherent Q2.

Spin rotations around at least two different axes are required to reach any point on the Bloch sphere. In Fig. 3a we demonstrate two-axis qubit control at both 1.5 K and 4.2 K by employing a Hahn-type echo sequence. A modulation of the relative phase ϕ of the second $\frac{\pi}{2}$-pulse yields a set of Ramsey fringes that are phase-shifted by π for a π_x and π_y echo pulse, which is applied to extend the coherence. The performance of the hole spin rotations is characterised using randomised benchmarking [42, 43] (see Fig. 3b and Methods). At 1.5 K, a single-qubit gate fidelity of $F_{\mathrm{s}} = 98.9 \pm 0.2\,\%$ is obtained, which is almost at the fault-tolerance level [3, 4] and very similar to the values recently reported for hot electron spin qubits [14, 15]. The fidelity is reduced to $F_{\mathrm{s}} = 98.6 \pm 1.6\,\%$ ($97.9 \pm 1.1\,\%$) at 3 K (4.2 K), revealing a similar scaling with temperature as T_2^*. We thus expect to be able to enhance the gate fidelities further by improving the qubit coherence, and by optimisation of the gate pulses [44].

Besides rotations around the x- and y-axis of the Bloch sphere, z-rotations can be realised by exploiting the electrical tunability of the qubit frequency (Fig. 1g). For this purpose a square pulse of amplitude A_{Z} and duration t_{Z} is added to a Hahn echo sequence (Fig. 3c) in order to rapidly detune the spin precession frequency, which leads to a phase pick up around the z-axis of the Bloch sphere [6]. As a consequence, the DQD current oscillates as a function of t_{Z} (Fig. 3d) at a frequency

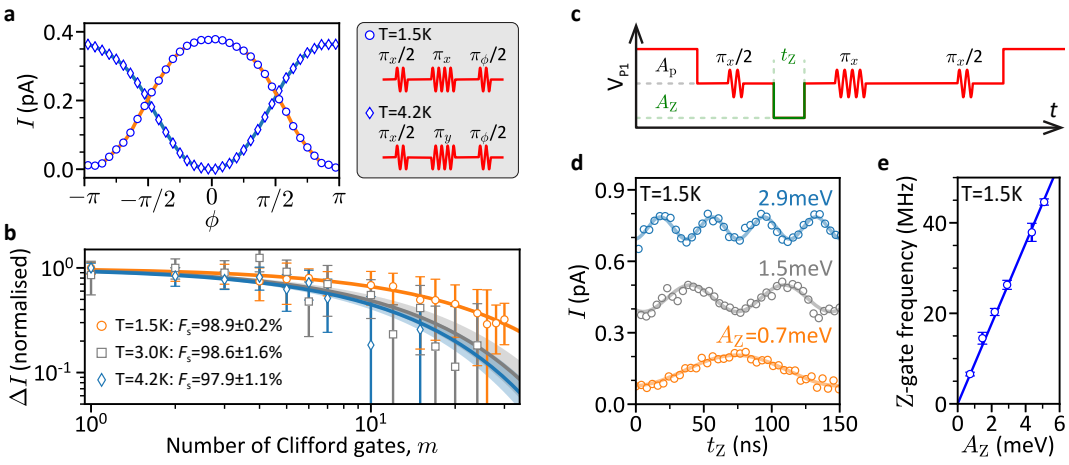

FIG. 3. **X, Y and Z qubit gates.** **a**, Demonstration of two-axis qubit control by applying a Hahn-type echo sequence, where the relative phase ϕ of the second $\frac{\pi}{2}$-pulse is varied. The measurements at 1.5 K (circles) and 4.2 K (diamonds) are phase-shifted by π due to the two orthogonal echo pulses, as shown in the right panel. **b**, Standard randomised benchmarking at 1.5 K (circles), 3 K (squares) and 4.2 K (diamonds) is performed by applying a varying number of Clifford gates m and preparing either a $|\uparrow\rangle$ or $|\downarrow\rangle$ final state. The normalised difference of currents is fitted to a single exponential decay to extract the single-qubit gate fidelities F_s (see Methods for further details). The shaded regions show the one-sigma error range of the fit parameters. The maximum m decreases with increasing temperature due to a reduced readout contrast. **c**, Schematic representation of the pulse scheme used to demonstrate qubit rotations around the z-axis of the Bloch sphere. In a modified Hahn echo sequence a square pulse of amplitude A_Z and duration t_Z is applied to shift the qubit precession frequency (see Fig. 1 g). The resulting phase-shift-induced oscillations are shown in **d** for different A_Z. Solid curves represent fits to a sinusoidal function, where the oscillation frequency is given by the induced qubit frequency shift. Traces are offset by an increment of 0.3 for clarity. **e**, The speed of the z-rotations increases linearly with A_Z. The solid line represents a linear fit to the data, yielding a frequency-shift of 8.9 MHz/meV. The data presented in this figure was taken for Q2 at $f_\mathrm{MW} = 8.812$ GHz.

that increases linearly with A_Z up to ~ 45 MHz (Fig. 3e).

Finally, in order to gain insight into the sources of decoherence we perform noise spectroscopy by employing Carr-Purcell-Meiboom-Gill (CPMG) pulse sequences [45], where a series of n_π π_y-pulses is applied as a spectral filter for the environmental noise [6, 46–48]. For a power-law noise spectrum $S(f) \propto f^{-\beta}$, the CPMG coherence time T_2^CPMG is expected to scale as $T_2^\mathrm{CPMG} \propto (n_\pi)^{\frac{\beta}{1+\beta}}$ [47]. This dependency is confirmed by Fig. 4a, and a β of 0.88 ± 0.11 (0.26 ± 0.03) is determined for 1.5 K (3 K), revealing a whitening of the noise on increasing the temperature and thus a reduced noise-decoupling efficiency. For $n_\pi = 32$ the hole spin coherence time is extended to 5.4 μs at 1.5 K, which corresponds to an increase by a factor of 27 compared to the unprotected qubit. While our CPMG

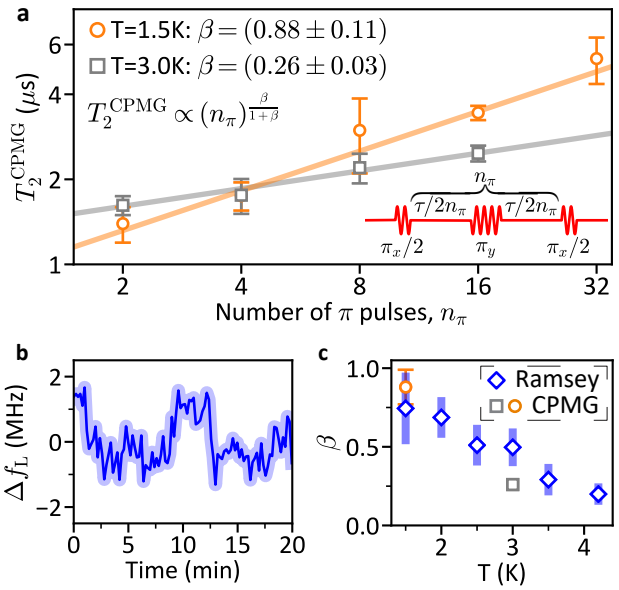

FIG. 4. **Dynamical decoupling and noise spectroscopy.** **a**, The spin coherence time can be enhanced by decoupling the qubit from low-frequency noise using a CPMG pulse sequence (see bottom-right schematic). A power-law dependence of the coherence time on the number of refocusing pulses n_π is confirmed by fitting (solid lines) the data to $T_2^{\mathrm{CPMG}} = T_2^0 (n_\pi)^{\frac{\beta}{1+\beta}}$, where β represents the scaling exponent of a power-law noise spectrum, $S(f) \propto f^{-\beta}$. **b**, Time trace of the qubit frequency obtained from repeated Ramsey measurements. The shaded region indicates the frequency uncertainty due to readout noise. **c**, Temperature dependence of the noise exponent β extracted from either CPMG or Ramsey measurements. The data presented in this figure was taken for Q2 at $f_{\mathrm{MW}} = 8.812\,\mathrm{GHz}$.

measurements are sensitive to the noise at frequencies of $f \sim 10^5 - 10^7$ Hz, we independently probe $S(f)$ at $f \sim 10^{-3} - 10^{-1}$ Hz by tracking the Larmor frequency fluctuations through repeated Ramsey experiments [6] (Fig. 4b). The temperature dependence of β demonstrates a noise whitening in both frequency ranges, and the good agreement of the β-values for the two frequency windows suggests a similar coloured noise spectrum over a wide range of frequencies. From the scaling of β with T we cannot uniquely identify the underlying noise sources, such as charge or nuclear spin fluctuations [49]. We note, however, that the longest T_2^* measured is ~ 440 ns (Supplementary Section 9), which does not only exceed the dephasing times reported so far for hole spins in Si at mK temperatures [50], but is also close to the estimated limit of ~ 500 ns set by the hole spin hyperfine interaction (Supplementary Section 10). This sub-μs limit is a consequence of the hole spins interacting with a relatively small number of nuclear spins $N_s \sim 310$, which increases the Overhauser field fluctuations that scale with $1/\sqrt{N_s}$ [51], and also represents a lower bound due the anisotropy of the hole hyperfine interaction [34].

In conclusion, we have demonstrated hole spin qubits in Si FinFETs that operate above 4 K. On the one hand, the strong SOI allows for spin rotations as fast as 147 MHz, and on the other hand, the weak hyperfine coupling ensures T_2^* up to 440 ns. In addition to two-axis control, we implement fast z-rotations by employing the electrical tunability of the g^*-factor. At 1.5 K we achieve nearly fault-tolerant single-qubit gate fidelities. These results have been accomplished using a fully CMOS-compatible FinFET device architecture, which is optimised for scalable integration, and therefore highlight the great potential of Si hole spin qubits for large-scale quantum computation.

In the quest for a higher qubit quality factor, hyperfine-induced dephasing can be prevented by engineering a nearly nuclear-spin-free environment [4]. While a stronger SOI results in shorter gate times, it also increases the susceptibility to charge noise. For hole spins in Si FinFETs, however, an unusually strong and at the same time electrically tunable SOI, allowing for on demand switching between qubit idling and manipulation modes, has been predicted [22, 23, 32].

Methods

Device fabrication. The fin structures are defined on a near-intrinsic Si substrate ($\rho > 10\,\mathrm{k\Omega cm}$, (100) surface) by means of electron-beam lithography (EBL) and dry etching [9]. The gate oxide is formed by thermal oxidation of the Si, yielding a $\simeq 7$ nm-thick silicon dioxide (SiO_2) layer, which is covered by $\simeq 20$ nm of titanium nitride (TiN) grown by atomic layer deposition (ALD). The first layer of gates containing L1, L2 and B is patterned using EBL and dry etching. Subsequently, the gate stack ($\simeq 4.5$ nm SiO_x, $\simeq 20$ nm TiN) of the second gate layer hosting P1 and P2 is grown by ALD. The plunger gates are implemented by means of a self-aligned process [10], where the gaps between the gates of the first gate layer (highlighted in turquoise in Fig. 1a) act as a template for the plungers gates. The gate lengths of the device measured are $l_\mathrm{B} \simeq 35$ nm and $l_\mathrm{P} \simeq 15$ nm. Source and drain contacts are p-type and made of platinum silicide (PtSi), which is formed by sputtering a $\simeq 15$ nm-thick Pt layer on a beforehand cleaned Si surface, followed by a silicidation anneal at 450 °C for 10 min in an argon ambient. Finally, the devices are encapsulated in a $\simeq 100$ nm-thick SiO_2 layer that is grown by plasma-enhanced chemical vapour deposition and are accessed via tungsten interconnects.

Experimental setup. All measurements are performed using a variable temperature insert that can be operated at $1.5 - 50$ K. MW and DC signals can be applied simultaneously to gate P1 (see Fig. 1b) via a bias-tee on the sample board. DC voltages are supplied by a low-noise voltage source (BasPI SP927) and the source-drain current is measured with a current-to-voltage amplifier at gain

10^9 (BasPI SP983c). A square voltage pulse used to drive the device between Coulomb blockade (qubit manipulation stage) and Pauli spin blockade (qubit initialisation and readout stage) is provided by an arbitrary waveform generator (Tektronix AWG5204), which also controls the I and Q inputs of a vector signal generator (Keysight E8267D) to generate phase-controlled MW bursts. The latter ones and the square pulse are combined using a wideband power combiner (Mini-Circuits ZC2PD-5R263-S+). The qubit readout current is distinguished from the background by chopping the MW signal at a frequency of 89.2 Hz and demodulating the current at this frequency with a lock-in amplifier (Signal Recovery 7265). For further details see supplementary information.

Clifford benchmarking protocol. Randomised benchmarking is performed by applying a randomised sequence of a varying number of Clifford gates m before the spin state is rotated such that the final state ideally becomes either the $|\uparrow\rangle$ or $|\downarrow\rangle$ state. Each of the 24 gates in the Clifford group is constructed from the set $\{\mathrm{I}, \pm\mathrm{X}, \pm\mathrm{Y}, \pm\mathrm{X}/2, \pm\mathrm{Y}/2\}$ [43]. Assuming that the qubit initial state is $|\downarrow\rangle$, a current flow is only observed when spin blockade is lifted for a final $|\uparrow\rangle$ state. Thus, the difference in current between sequences designed to output either a $|\uparrow\rangle$ or $|\downarrow\rangle$ state, $\Delta\mathrm{I} = \mathrm{I}^{|\uparrow\rangle} - \mathrm{I}^{|\downarrow\rangle}$, is proportional to $p_\uparrow^{|\uparrow\rangle} - p_\uparrow^{|\downarrow\rangle}$. For each m we average over 10 randomised sequences and the average Clifford-gate fidelity F_c is obtained from fitting the normalised current difference to $(2F_\mathrm{c} - 1)^m$. Since a Clifford gate consists of on average 1.875 gates, the average single-qubit gate fidelity F_s is derived by $F_\mathrm{s} = 1 - (1 - F_\mathrm{c})/1.875$.

Acknowledgements

We thank M. de Kruijf, C. Kloeffel, D. Loss, F. Froning and F. Braakman for fruitful discussions. Moreover, we acknowledge support by the cleanroom operation team, in particular by U. Drechsler, A. Olziersky and D. Davila Pineda, at the IBM Binnig and Rohrer Nanotechnology Center, as well as technical support at the University of Basel by S. Martin and M. Steinacher. This work was partially supported by the Georg H. Endress Foundation, the NCCR SPIN, the Swiss Nanoscience Institute (SNI), the Swiss NSF (grant nr. 179024), and the EU H2020 European Microkelvin Platform EMP (grant nr. 824109). L.C.C. acknowledges support by a Swiss NSF mobility fellowship (P2BSP2_200127).

Author contributions

A.V.K., L.C.C., S.G., A.F., R.J.W. and D.M.Z. conceived the project and experiments. A.V.K. and S.G. fabricated the device. L.C.C. and D.M.Z. prepared the cryogenic measurement setup.

A.V.K. S.G., L.C.C. and D.M.Z. performed the experiments. A.V.K, L.C.C., and S.G. analysed the data and wrote the manuscript with input from all the authors.

Competing interests

The authors declare no competing interests.

---

[1] D. Loss and D. P. DiVincenzo, Quantum computation with quantum dots, Physical Review A **57**, 120 (1998).

[2] C. Kloeffel and D. Loss, Prospects for Spin-Based Quantum Computing in Quantum Dots, Annual Review of Condensed Matter Physics **4**, 51 (2013).

[3] A. G. Fowler, M. Mariantoni, J. M. Martinis, and A. N. Cleland, Surface codes: Towards practical large-scale quantum computation, Phys. Rev. A **86**, 032324 (2012).

[4] M. Veldhorst, J. C. C. Hwang, C. H. Yang, A. W. Leenstra, B. de Ronde, J. P. Dehollain, J. T. Muhonen, F. E. Hudson, K. M. Itoh, A. Morello, and A. S. Dzurak, An addressable quantum dot qubit with fault-tolerant control-fidelity, Nature Nanotechnology **9**, 981 (2014).

[5] K. Takeda, J. Kamioka, T. Otsuka, J. Yoneda, T. Nakajima, M. R. Delbecq, S. Amaha, G. Allison, T. Kodera, S. Oda, and S. Tarucha, A fault-tolerant addressable spin qubit in a natural silicon quantum dot, Science Advances **2**, e1600694 (2016).

[6] J. Yoneda, K. Takeda, T. Otsuka, T. Nakajima, M. R. Delbecq, G. Allison, T. Honda, T. Kodera, S. Oda, Y. Hoshi, N. Usami, K. M. Itoh, and S. Tarucha, A quantum-dot spin qubit with coherence limited by charge noise and fidelity higher than 99.9%, Nature Nanotechnology **13**, 102 (2017).

[7] C. H. Yang, K. W. Chan, R. Harper, W. Huang, T. Evans, J. C. C. Hwang, B. Hensen, A. Laucht, T. Tanttu, F. E. Hudson, S. T. Flammia, K. M. Itoh, A. Morello, S. D. Bartlett, and A. S. Dzurak, Silicon qubit fidelities approaching incoherent noise limits via pulse engineering, Nature Electronics **2**, 151 (2019).

[8] R. Maurand, X. Jehl, D. Kotekar-Patil, A. Corna, H. Bohuslavskyi, R. Laviéville, L. Hutin, S. Barraud, M. Vinet, M. Sanquer, and S. D. Franceschi, A CMOS silicon spin qubit, Nature Communications **7**, 13575 (2016).

[9] A. V. Kuhlmann, V. Deshpande, L. C. Camenzind, D. M. Zumbühl, and A. Fuhrer, Ambipolar quantum dots in undoped silicon fin field-effect transistors, Applied Physics Letters **113**, 122107 (2018).

[10] S. Geyer, L. C. Camenzind, L. Czornomaz, V. Deshpande, A. Fuhrer, R. J. Warburton, D. M. Zumbühl, and A. V. Kuhlmann, Silicon quantum dot devices with a self-aligned second gate layer, arXiv:2007.15400 (2020).

[11] L. M. K. Vandersypen, H. Bluhm, J. S. Clarke, A. S. Dzurak, R. Ishihara, A. Morello, D. J. Reilly,

L. R. Schreiber, and M. Veldhorst, Interfacing spin qubits in quantum dots and donors—hot, dense, and coherent, npj Quantum Information **3**, 24 (2017).

[12] M. Veldhorst, H. G. J. Eenink, C. H. Yang, and A. S. Dzurak, Silicon CMOS architecture for a spin-based quantum computer, Nature Communications **8**, 1766 (2017).

[13] D. Franke, J. Clarke, L. Vandersypen, and M. Veldhorst, Rent's rule and extensibility in quantum computing, Microprocessors and Microsystems **67**, 1 (2019).

[14] L. Petit, H. G. J. Eenink, M. Russ, W. I. L. Lawrie, N. W. Hendrickx, S. G. J. Philips, J. S. Clarke, L. M. K. Vandersypen, and M. Veldhorst, Universal quantum logic in hot silicon qubits, Nature **580**, 355 (2020).

[15] C. H. Yang, R. C. C. Leon, J. C. C. Hwang, A. Saraiva, T. Tanttu, W. Huang, J. C. Lemyre, K. W. Chan, K. Y. Tan, F. E. Hudson, K. M. Itoh, A. Morello, M. Pioro-Ladrière, A. Laucht, and A. S. Dzurak, Operation of a silicon quantum processor unit cell above one kelvin, Nature **580**, 350 (2020).

[16] X. Xue, B. Patra, J. P. G. van Dijk, N. Samkharadze, S. Subramanian, A. Corna, C. Jeon, F. Sheikh, E. Juarez-Hernandez, B. P. Esparza, H. Rampurawala, B. Carlton, S. Ravikumar, C. Nieva, S. Kim, H.-J. Lee, A. Sammak, G. Scappucci, M. Veldhorst, F. Sebastiano, M. Babaie, S. Pellerano, E. Charbon, and L. M. K. Vandersypen, CMOS-based cryogenic control of silicon quantum circuits, arXiv:2009.14185 (2020).

[17] E. Kawakami, P. Scarlino, D. R. Ward, F. R. Braakman, D. E. Savage, M. G. Lagally, M. Friesen, S. N. Coppersmith, M. A. Eriksson, and L. M. K. Vandersypen, Electrical control of a long-lived spin qubit in a Si/SiGe quantum dot, Nature Nanotechnology **9**, 666 (2014).

[18] D. V. Bulaev and D. Loss, Spin Relaxation and Decoherence of Holes in Quantum Dots, Physical Review Letters **95**, 076805 (2005).

[19] H. Watzinger, J. Kukučka, L. Vukušić, F. Gao, T. Wang, F. Schäffler, J.-J. Zhang, and G. Katsaros, A germanium hole spin qubit, Nature Communications **9**, 3902 (2018).

[20] N. W. Hendrickx, W. I. L. Lawrie, L. Petit, A. Sammak, G. Scappucci, and M. Veldhorst, A single-hole spin qubit, Nature Communications **11**, 3478 (2020).

[21] N. W. Hendrickx, W. I. L. Lawrie, M. Russ, F. van Riggelen, S. L. de Snoo, R. N. Schouten, A. Sammak, G. Scappucci, and M. Veldhorst, A four-qubit germanium quantum processor, arXiv:2009.04268 (2020).

[22] F. N. M. Froning, L. C. Camenzind, O. A. H. van der Molen, A. Li, E. P. A. M. Bakkers, D. M. Zumbühl, and F. R. Braakman, Ultrafast hole spin qubit with gate-tunable spin–orbit switch functionality, Nature Nanotechnology 10.1038/s41565-020-00828-6 (2021).

[23] C. Kloeffel, M. J. Rančić, and D. Loss, Direct Rashba spin-orbit interaction in Si and Ge nanowires with different growth directions, Physical Review B **97**, 235422 (2018).

[24] V. N. Golovach, M. Borhani, and D. Loss, Electric-dipole-induced spin resonance in quantum dots, Physical Review B **74**, 165319 (2006).

[25] K. C. Nowack, F. H. L. Koppens, Y. V. Nazarov, and L. M. K. Vandersypen, Coherent Control of a Single Electron Spin with Electric Fields, Science **318**, 1430 (2007).

[26] D. V. Bulaev and D. Loss, Electric Dipole Spin Resonance for Heavy Holes in Quantum Dots, Physical Review Letters **98**, 097202 (2007).

[27] S. Nadj-Perge, S. M. Frolov, E. P. A. M. Bakkers, and L. P. Kouwenhoven, Spin–orbit qubit in a semiconductor nanowire, Nature **468**, 1084 (2010).

[28] Y. Kato, Gigahertz Electron Spin Manipulation Using Voltage-Controlled g-Tensor Modulation, Science **299**, 1201 (2003).

[29] N. Ares, G. Katsaros, V. N. Golovach, J. J. Zhang, A. Prager, L. I. Glazman, O. G. Schmidt, and S. D. Franceschi, SiGe quantum dots for fast hole spin Rabi oscillations, Applied Physics Letters **103**, 263113 (2013).

[30] B. Voisin, R. Maurand, S. Barraud, M. Vinet, X. Jehl, M. Sanquer, J. Renard, and S. D. Franceschi, Electrical control of g-factor in a few-hole silicon nanowire MOSFET, Nano Letters **16**, 88 (2015).

[31] A. Crippa, R. Maurand, L. Bourdet, D. Kotekar-Patil, A. Amisse, X. Jehl, M. Sanquer, R. Laviéville, H. Bohuslavskyi, L. Hutin, S. Barraud, M. Vinet, Y.-M. Niquet, and S. D. Franceschi, Electrical Spin Driving by g -Matrix Modulation in Spin-Orbit Qubits, Physical Review Letters **120**, 137702 (2018).

[32] S. Bosco, B. Hetényi, and D. Loss, Hole spin qubits in Si FinFETs with fully tunable spin-orbit coupling and sweet spots for charge noise, arXiv:2011.09417 (2020).

[33] A. V. Khaetskii, D. Loss, and L. Glazman, Electron Spin Decoherence in Quantum Dots due to Interaction with Nuclei, Physical Review Letters **88**, 186802 (2002).

[34] J. H. Prechtel, A. V. Kuhlmann, J. Houel, A. Ludwig, S. R. Valentin, A. D. Wieck, and R. J. Warburton, Decoupling a hole spin qubit from the nuclear spins, Nature Materials **15**, 981 (2016).

[35] A. M. J. Zwerver, T. Krähenmann, T. F. Watson, L. Lampert, H. C. George, R. Pillarisetty, S. A. Bojarski, P. Amin, S. V. Amitonov, J. M. Boter, R. Caudillo, D. Corras-Serrano, J. P. Dehollain, G. Droulers, E. M. Henry, R. Kotlyar, M. Lodari, F. Luthi, D. J. Michalak, B. K. Mueller, S. Neyens, J. Roberts, N. Samkharadze, G. Zheng, O. K. Zietz, G. Scappucci, M. Veldhorst, L. M. K. Vandersypen, and J. S. Clarke, Qubits made by advanced semiconductor manufacturing, arXiv:2101.12650 (2021).

[36] K. Ono, D. Austing, Y. Tokura, and S. Tarucha, Current Rectification by Pauli Exclusion in a Weakly Coupled Double Quantum Dot System, Science **297**, 1313 (2002).

[37] A. C. Johnson, J. R. Petta, C. M. Marcus, M. P. Hanson, and A. C. Gossard, Singlet-triplet spin blockade and charge sensing in a few-electron double quantum dot, Physical Review B **72**, 165308 (2005).

[38] M. Field, C. G. Smith, M. Pepper, D. A. Ritchie, J. E. F. Frost, G. A. C. Jones, and D. G. Hasko, Measurements of Coulomb blockade with a noninvasive voltage probe, Physical Review Letters **70**, 1311 (1993).

[39] R. Hanson, L. P. Kouwenhoven, J. R. Petta, S. Tarucha, and L. M. K. Vandersypen, Spins in few-electron quantum dots, Reviews of Modern Physics **79**, 1217 (2007).

[40] J. M. Elzerman, R. Hanson, L. H. W. van Beveren, B. Witkamp, L. M. K. Vandersypen, and L. P. Kouwenhoven, Single-shot read-out of an individual electron spin in a quantum dot, Nature **430**, 431

(2004).

[41] T. F. Watson, S. G. J. Philips, E. Kawakami, D. R. Ward, P. Scarlino, M. Veldhorst, D. E. Savage, M. G. Lagally, M. Friesen, S. N. Coppersmith, M. A. Eriksson, and L. M. K. Vandersypen, A programmable two-qubit quantum processor in silicon, Nature **555**, 633 (2018).

[42] E. Knill, D. Leibfried, R. Reichle, J. Britton, R. B. Blakestad, J. D. Jost, C. Langer, R. Ozeri, S. Seidelin, and D. J. Wineland, Randomized benchmarking of quantum gates, Physical Review A **77**, 012307 (2008).

[43] J. T. Muhonen, A. Laucht, S. Simmons, J. P. Dehollain, R. Kalra, F. E. Hudson, S. Freer, K. M. Itoh, D. N. Jamieson, J. C. McCallum, A. S. Dzurak, and A. Morello, Quantifying the quantum gate fidelity of single-atom spin qubits in silicon by randomized benchmarking, Journal of Physics: Condensed Matter **27**, 154205 (2015).

[44] J. Kelly, R. Barends, B. Campbell, Y. Chen, Z. Chen, B. Chiaro, A. Dunsworth, A. Fowler, I.-C. Hoi, E. Jeffrey, A. Megrant, J. Mutus, C. Neill, P. O'Malley, C. Quintana, P. Roushan, D. Sank, A. Vainsencher, J. Wenner, T. White, A. Cleland, and J. M. Martinis, Optimal Quantum Control Using Randomized Benchmarking, Physical Review Letters **112**, 240504 (2014).

[45] S. Meiboom and D. Gill, Modified Spin-Echo Method for Measuring Nuclear Relaxation Times, Review of Scientific Instruments **29**, 688 (1958).

[46] J. Bylander, S. Gustavsson, F. Yan, F. Yoshihara, K. Harrabi, G. Fitch, D. G. Cory, Y. Nakamura, J.-S. Tsai, and W. D. Oliver, Noise spectroscopy through dynamical decoupling with a superconducting flux qubit, Nature Physics **7**, 565 (2011).

[47] J. Medford, Ł. Cywiński, C. Barthel, C. M. Marcus, M. P. Hanson, and A. C. Gossard, Scaling of Dynamical Decoupling for Spin Qubits, Physical Review Letters **108**, 086802 (2012).

[48] F. K. Malinowski, F. Martins, P. D. Nissen, E. Barnes, Ł. Cywiński, M. S. Rudner, S. Fallahi, G. C. Gardner, M. J. Manfra, C. M. Marcus, and F. Kuemmeth, Notch filtering the nuclear environment of a spin qubit, Nature Nanotechnology **12**, 16 (2016).

[49] A. V. Kuhlmann, J. Houel, A. Ludwig, L. Greuter, D. Reuter, A. D. Wieck, M. Poggio, and R. J. Warburton, Charge noise and spin noise in a semiconductor quantum device, Nature Physics **9**, 570 (2013).

[50] L. Hutin, B. Bertrand, R. Maurand, A. Crippa, M. Urdampilleta, Y. Kim, A. Amisse, H. Bohuslavskyi, L. Bourdet, S. Barraud, X. Jeh, Y.-M. Niquet, M. Sanquer, C. Bauerle, T. Meunier, S. D. Franceschi, and M. Vinet, Si MOS technology for spin-based quantum computing, in *2018 48th European Solid-State Device Research Conference (ESSDERC)* (IEEE, 2018).

[51] L. V. C. Assali, H. M. Petrilli, R. B. Capaz, B. Koiller, X. Hu, and S. D. Sarma, Hyperfine interactions in silicon quantum dots, Physical Review B **83**, 165301 (2011).